Heliyon 8 (2022) e09883

Contents lists available at ScienceDirect

Heliyon

journal homepage: www.cell.com/heliyon

Research article

A multi-perspective analysis of microclimate dynamics for air-based solar hydrogen production

Foster Lubbe [a,*], Jacques Maritz [b], Tom Bosserez [a], Jan Rongé [a], Johan A. Martens [a]

[a] Centre for Surface Chemistry and Catalysis, KU Leuven, Celestijnenlaan 200f, Leuven, 3001, Belgium
[b] Department of Engineering Sciences, University of the Free State, P.O. Box 339, Bloemfontein, 9300, South Africa

HIGHLIGHTS

- Decentralized hydrogen production.
- Temperature and humidity at different heights above the ground.
- Statistical characterization of a microclimate.
- Microclimate analysis.
- Wavelet Transform Coherence analysis.

GRAPHICAL ABSTRACT

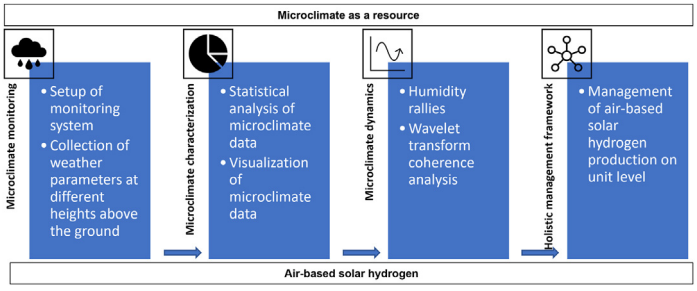

ARTICLE INFO

Keywords:
Decentralized hydrogen production
Temperature and humidity at different heights above the ground
Statistical characterization of a microclimate
Microclimate analysis
Wavelet transform coherence

ABSTRACT

Navigating the microclimatic environment for the optimal control of water-from-air devices could be a challenge. An example of such a device is an air-based solar hydrogen production device. Such a device promises the ability for off-grid, easily deployable and modular hydrogen production for on-site consumption. Novel analysis techniques, such as wavelet transform coherence analysis, could assist in better understanding the microclimate in which air-based hydrogen production devices might function. The analysis becomes complicated when a system is evaluated at the microclimatic level, especially when it is considered that the performance of air-based solar hydrogen devices are not only dependent on solar radiation, but also on humidity levels in the air. To get a grasp of the interactions that take place within a microclimatic system, a two-tiered approach is presented. It has been shown that relative humidity and temperature is stratified close to the ground, and that the stratification undergoes an inversion twice per day. A possible link between absolute humidity and wind direction is observed and humidity rallies are identified. Using microclimate monitoring and wavelet transform coherence analysis, an attempt is made to disentangle microclimatic variables by pointing out regions of high coherence and regions of low coherence between different variables. It is furthermore suggested that the propagation direction of a humidification process within the microclimate can be determined by considering the phase angle between relative humidity timeseries at different heights above the ground, using wavelet transform coherence analysis. It has been demonstrated that wavelet transform coherence analysis, in conjunction with a comprehensive microclimate monitoring process, could support the understanding of the complex processes that occur within the microclimatic environment and therefore support the management of water-from-air systems. In this regard a management framework is also presented.

* Corresponding author.
E-mail address: foster.lubbe@kuleuven.be (F. Lubbe).

https://doi.org/10.1016/j.heliyon.2022.e09883
Received 20 April 2022; Received in revised form 25 May 2022; Accepted 1 July 2022

1. Introduction

Solar energy is the most abundant clean energy source available on earth, with 120 000 TW of solar power reaching the earth's surface on a continuous basis (Van De Krol, Liang and Schoonman, 2008). However, the intermittent nature of renewable energy sources gives rise to challenges with regards to grid stability (Pinaud et al., 2013; Rongé et al., 2015; Bhandari and Shah, 2021). Therefore, in order to fully tap into this resource, it is important that solar energy can be stored efficiently (Van De Krol, Liang and Schoonman, 2008; Bhandari and Shah, 2021; International Energy Agency, 2021). This challenge can be addressed by making use of chemical fuels synthesized using renewable energy. Hydrogen is particularly attractive as a solar fuel due to its high mass energy density, appropriateness for seasonal storage, and its versatility to be used across various industries and applications (Pinaud et al., 2013; Rongé et al., 2015; Bhandari and Shah, 2021). In fact, hydrogen is seen as a key component in the quest to decarbonize hard to abate sectors of the global economy (Hydrogen Europe, 2019; Bhandari and Shah, 2021; International Energy Agency, 2021). According to the industry and research association Hydrogen Europe, hydrogen will enable 'the most thorough decarbonization scheme the world has ever seen'. Industrial growth for the use of hydrogen in sectors beyond mobility has indeed been significant (Hydrogen Europe, 2019).

Producing hydrogen directly from sunlight eliminates inefficiencies associated with electricity production and transmission and allows for operation at lower current densities, further increasing energy conversion efficiency (Van De Krol, Liang and Schoonman, 2008). An integrated device that produces hydrogen directly from solar energy also guarantees that hydrogen is produced from a renewable energy source (as opposed to an electrolyser connected to an electricity grid which might be only partially supplied by renewable energy).

Electricity production and water consumption is intricately linked. Climate change and industry reform in recent years has led to an intensification of the interaction between water and energy - the effects of which are felt all over the world (Hamiche et al., 2016). In fact, water scarcity could hamper energy security in some parts of the world (Miletto, 2015; Hamiche et al., 2016). It is therefore important to find a solution to decouple the water-energy-nexus in the hydrogen production process. Not only is liquid water a feedstock in water electrolysis, but the water-energy-nexus is aggravated when electricity from thermoelectric power plants is used (Hamiche et al., 2016; Peeters et al., 2021). An integrated, modular system that produces hydrogen from the moisture in the air, using solar energy directly, could significantly weaken the coupling between water and energy (Rongé et al., 2015). Furthermore, a decentralized, vapour-fed, integrated hydrogen device could address all three factors of the energy trilemma, namely energy security, energy equity, and environmental sustainability. Such a device could also address existing problems associated with solar hydrogen production, such as sub-optimal water purity, water scarcity in high solar radiation areas, complicated system architecture that includes pumps, tubing, and filters, as well as high costs associated with complex systems (Rongé et al., 2015).

In 2017 Heremans et al. (2017) published a paper announcing the achievement of a world-record efficiency of 15% for a vapour-fed solar hydrogen device. This efficiency was achieved using earth-abundant catalysts, potentially lowering the cost of an air-to-hydrogen device and opening perspectives for the development of scaled-up, robust, green hydrogen-from-air devices (Rongé et al., 2015; Heremans et al., 2017).

The expansion of green hydrogen production, in general, faces the challenge of varying ambient conditions such as solar radiation and wind speed (Bhandari and Shah, 2021). This challenge becomes even more important when the feedstock to hydrogen production is water vapour from the air, as ambient relative humidity and air temperature plays a significant role in the availability of water vapour.

Prominent studies on water-from-air technologies do not focus on the development of a control strategy for these technologies (Lord et al., 2021; Peeters et al., 2021). Furthermore, Bramer et al. (2018) point out that there is a need for more data on the vertical energy profile near the earth's surface, while climate envelope models do not sufficiently account for small-scale climate variations. Some studies also make use of unreliable, low-quality data loggers and sensors (Bramer et al., 2018). This article attempts to contribute in addressing these challenges.

In order to ascertain the feasibility of decentralized air-based solar hydrogen production at a specific location, the microclimatic resource should be carefully monitored. A weather station was established on a farm in the Western Cape in South Africa and a two-tiered system for the investigation of microclimate dynamics is developed.

The two-tiered system consists of the monitoring of weather data at four different heights above the ground and a wavelet transform coherence analyses. The result of this system of analysis is a better understanding of the dynamics and patterns that exist between different climatic variables in the microclimate, in order to inform control strategies for decentralized air-based hydrogen production.

Humidity rallies are identified and relative humidity and temperature are presented at heights of 10 cm, 45 cm, 80 cm and 115 cm above the ground.

Finally, the results of the two-tiered analysis of the microclimate are discussed in the context of the optimization and control of water-from-air devices under the influence of microclimatic factors.

Although the weather data used in this study has been collected at one specific site, the methodology developed in the paper is not site-specific. The weather data therefore serves a dual purpose. Firstly, phenomena such as temperature and humidity stratification, the influence of wind direction on absolute humidity, and site-specific humidity rallies are analysed and discussed. It could be noted that the stratification of temperature close to the ground has also been observed in other datasets, albeit not as pronounced as in the present study (Morecroft et al., 1998; Yang et al., 2013). Secondly, the weather data is used to demonstrate the proposed outline of a universal strategy that could be applied to weather data in order to manage water-from-air devices.

2. Materials and methods

2.1. Weather station

The microclimate monitoring system consists of two separate installations: a stand containing the electronics box (which contains the battery, data logger and modem), the solar panel and a ClimaVUE50 integrated weather sensor, as well as a stand containing four equally spaced relative humidity/temperature sensors and a camera. For the sake of simplicity the first stand described above will be referred to as the *climavue* and the second stand will be referred to as the *humidity stack*. These two installations are spaced three meters apart and connected via an underground cable. The complete installation can be seen in Figure 1 and Figure 2.

The complete microclimate monitoring system consists of the sensors described in Table 1.

2.2. Weather monitoring

Using the microclimate monitoring system, the weather was monitored at different heights above the ground. Weather data was logged at 10-minute intervals using a Campbell Scientific CR310 datalogger.

2.3. Statistical characterization using Python

Python was used to analyse the weather data. The Pandas package was use to structure the data and the Numpy package was used to perform a statistical analysis. Matplotlib was used to plot the resulting figures.

2.4. Wavelet transform coherence analysis

Wavelet analysis (WA) is a relatively new mathematical technique, evolving since its appearance in the thesis of Alfred Haar (1910). It was further developed by Yves Meyer (Daubechies et al., 1986) in the 1980s. The highly applicable feature of wavelet analysis lies in its elegant decomposition and coherence properties in both time and frequency space. This is different from the Fourier techniques which assume signals with stationary components, i.e. signals that contain frequencies that do not evolve. The wavelet analysis paradigm is governed by two main variants: continuous and discrete wavelet transforms (CWT and DWT), of which the latter finds applications in filter design (Penedo et al., 2019).

However, to aid the core purpose of this paper, the focus is on the CWT and its ability to perform feature extraction in both the time and frequency domain. Furthermore, to facilitate the process of comparing features, the wavelet transform coherence (WTC) is often used to search for high correlation of features across different datasets in both the time and frequency domain.

Several successful implementations of WTC exist within the framework of comparing several natural time series phenomena in both the time and frequency domain. These implementations range from coherence studies of electricity demand and weather data (Bonkaney et al., 2019), arctic oscillation index and Baltic maximum sea ice score (Grinsted et al., 2004), freshwater discharge and microclimate (Labat, 2010), and computational expansions towards including machine learning and artificial intelligence techniques in mid-to long term electric load forecasting (Zhang and Liu, 2010).

Assuming two time series, T_1 and T_2, representing some fundamental elements of a microclimate, for example temperature and relative humidity, the WTC could be constructed using the following strategy (Bonkaney et al., 2019):

$$WTC = \frac{|WA(T_1 T_2)|^2}{|T_1|^2 |T_2|^2} \tag{1}$$

and

Figure 1. The climavue consisting of an integrated weather sensor at the top, a solar panel, and a cabinet containing the battery, data logger and modem.

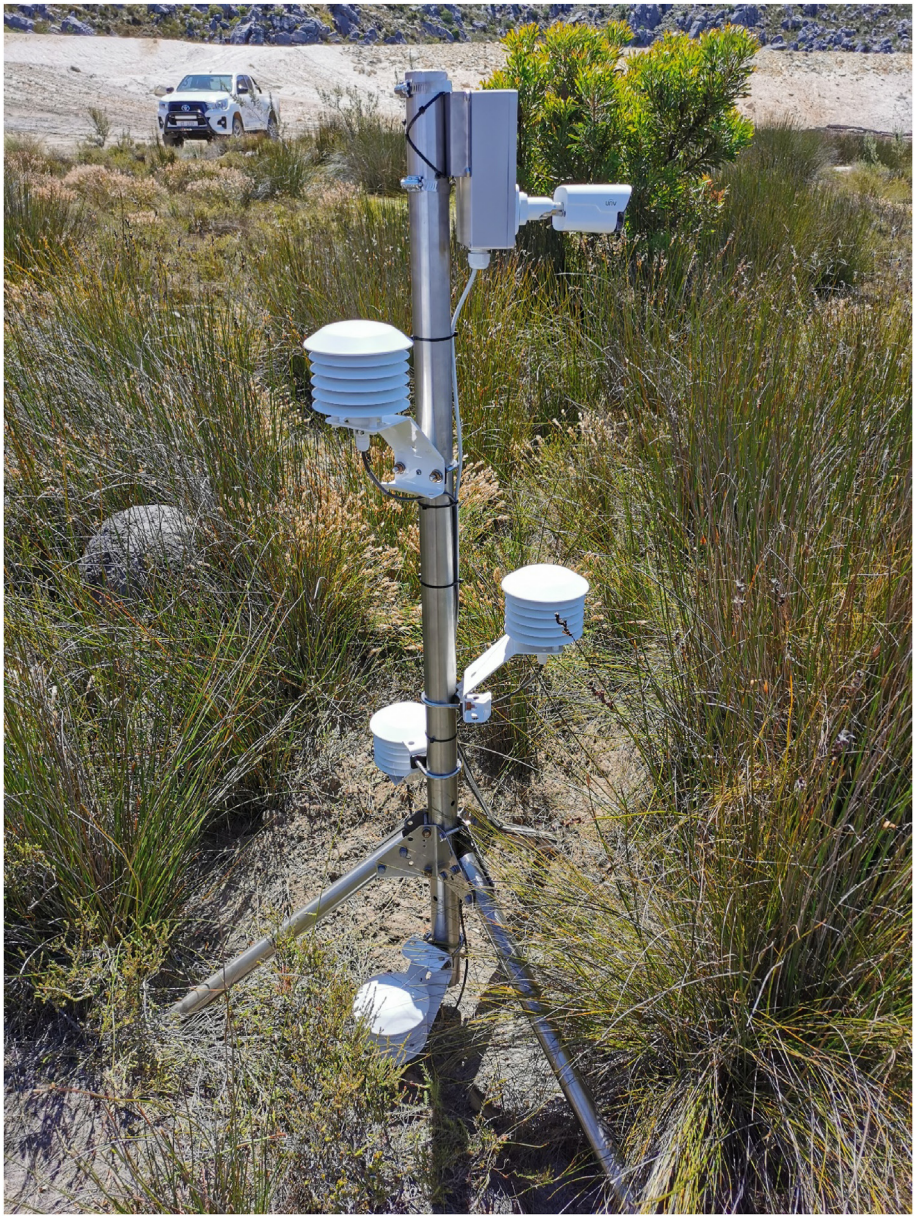

Figure 2. The humidity stack containing four equally spaced relative humidity/temperature sensors and a camera.

$$\Delta Phase = Phase(T_1) - Phase(T_2), \quad (2)$$

with $|WA(T_1T_2)|^2$, $|T_1|^2$, and $\Delta Phase$ representing the power of the wavelet analysis of two signals, the power of individual signals, and the phase difference between two signals. Eqs. (1) and (2) drive the ability to find instances of high coherence and phase information between two signals in both time and frequency domains.

The WTC is practically illustrated to the reader by using an explanatory result of applying WTC to two signals, which in this case, are two identical microclimate signals (Figure 3).

From Figure 3 it can be seen that both input signals of the WTC are identical, based on identical levels of coherence and identical phasor information (across all domains) that can be seen in the figure. The phasor information can be extracted by using the orientation of the arrows: right-pointing arrows indicate in-phase phenomena. For this article, WTC analysis was implemented using R.

3. Results and discussion

3.1. Characterization of the microclimatic resource

In order to assess the amount of hydrogen that can be produced by an air-based solar hydrogen device, the microclimatic resource must be characterized. This is the first task after weather station installation. Air temperature, relative humidity, solar radiation and windspeed are the most important for determining the potential of air-based solar hydrogen production.

To this end, Figure 4 shows the air temperature, relative humidity and solar radiation as a function of time for the year 2021 at the test site. Evaluation of these three parameters is the starting point for the evaluation of a microclimatic resource for air-based solar hydrogen production.

Table 1. Description of sensors of the microclimate monitoring system used in the study.

Sensor	Parameter measured	Height above ground (cm)	Integration	Range	Accuracy
Thermistor	Air temperature	200	Climavue	-50 to 60 °C	±0.6 °C
Digital temperature	Air temperature	10, 45, 80, 115	Humidity stack	-40 to 70 °C	±0.2 °C
Relative humidity	Relative humidity	200	Climavue	0–100%	±3%
Digital relative humidity	Relative humidity	10, 45, 80, 115	Humidity stack	0–100%	±1.5%
Silicon-cell pyranometer	Global horizontal solar irradiance	200	Climavue	0–1750 W/ m^{-2}	±5%
Ultrasonic anemometer	Wind speed	200	Climavue	0–30 m/s	±3%
Ultrasonic anemometer	Wind direction	200	Climavue	0–359°	±5°
Barometric pressure	Barometric pressure	200	Climavue	500 to 1100 hPa	±1 mb
	Vapour pressure	200	Climavue	0–47 kPa	±0.2 kPa
Water droplet counter	Precipitation	200	Climavue	0–400 mm/h	±5%
Tilt	Tilt	200	Climavue	-90 to 90°	±1°
Lightning	Lightning strike count	200	Climavue	0 to 65535 strikes	>25% detection at distance <10 km
Lightning	Lightning strike distance	200	Climavue	0–40 km	

In order to further characterize the microclimatic conditions, distributions of air temperature, relative humidity and windspeed are provided.

Figure 5 indicates the distribution of air temperature at the test site during the year 2021. This figure can be used to evaluate the suitability of the climatic extremes for air-based solar hydrogen production. It also gives an overview of the statistical evolution of air temperature during the year. Furthermore, the data has been split between daytime and night-time, adding a temporal dimension to the data visualization. As will be seen further on in the paper, temporal effects are an important factor to consider when managing air-based solar hydrogen production.

Relative humidity is a very important parameter for the evaluation of a site for air-based solar hydrogen production. It is not just important to have an overview, such as given in Figure 4, but a statistical representation of the data is also needed to determine the extremities. This representation can be seen in Figure 6. It is also recommended that such a representation is divided between daytime and night-time, in order to provide the hydrogen plant manager with temporal data.

When it comes to air-based solar hydrogen production, wind speed and direction could play an important role when developing an optimal control strategy, since it affects that rate at which moisture is carried into the microclimatic system. This can be seen in Figure 7 and Figure 8. Figure 7 illustrates the subset of wind data for absolute humidity values above the third quartile, i.e. high absolute humidity values, while Figure 8 illustrates the subset of wind data for absolute humidity values below the first quartile. For low absolute humidity values, wind from the south-east is more prominent than it is for high absolute humidity values.

Although not reported here, precipitation could also an important factor to be taken into account when developing a control strategy for an air-based solar hydrogen device, since it is a source of liquid water for the microclimate which could evaporate at a later stage to feed the air-based hydrogen device.

3.2. Characterization of microclimate dynamics

In Section 3.1, the distribution of weather data over one-month periods was used to characterize the climatic resource. The distributions provide an overview of the climate in a concise way and allow for comparison with other locations. However, some information remains hidden. Interesting phenomena occur at short time-scales and it is worthwhile to consider some of the climate dynamics at a higher resolution.

3.2.1. Humidity rallies

Figure 9 is a plot of the absolute humidity versus time for the period 1 January to 31 March 2021. Two periods are highlighted in grey, indicating what could be termed 'humidity rallies': a strong upward trend in absolute humidity over a couple of days. The two rallies that will be examined in more detail occurred between 2021/01/01 08:00:00 and 2021/01/05 09:00:00, and between 2021/03/09 00:00:00 and 2021/03/10 23:00:00.

Figure 10, top left, illustrates the first humidity rally. The absolute humidity increases from a minimum of 5 g/m^3 on 1 January to a value of 15 g/m^3 on 5 January. This rally is accompanied by an increase in relative humidity. The absolute humidity, however, does not mimic the day-night cycle as directly as is the case with relative humidity. Both the daytime and night-time maximum air temperature increases during the first three days of the rally, but stays fairly constant over the last two days. The fact that air temperature increases, while relative humidity also increases over this 5-day period, could indicate the influx of moisture from a source external to the microclimate. Solar radiation remains fairly smooth for the first three days and peaks at around 1100 W/m^2. On the

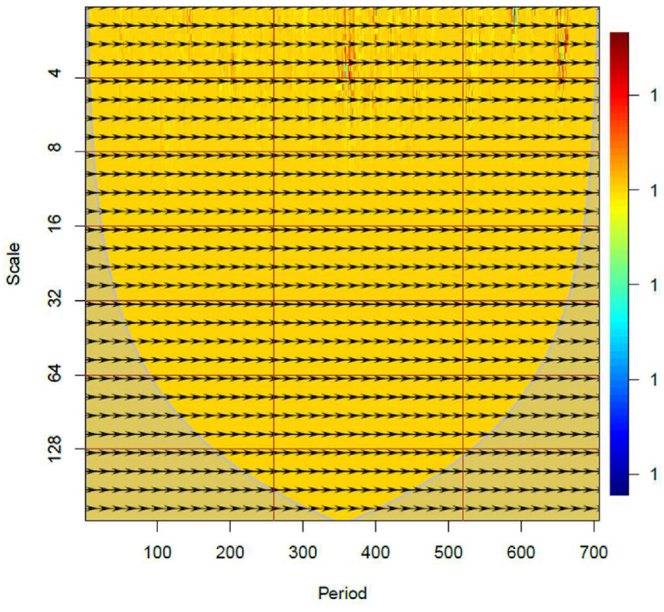

Figure 3. WTC of two identical relative humidity signals. WA scales (relatable to period of oscillations), duration of dataset and level of coherence in power are indicated on the x, y and z axis, respectively. The cone of confluence is also indicated. Arrows indicate phasor information. WA scales relate to the compression of the wavelet and small and large scales resemble short and long-term dynamics.

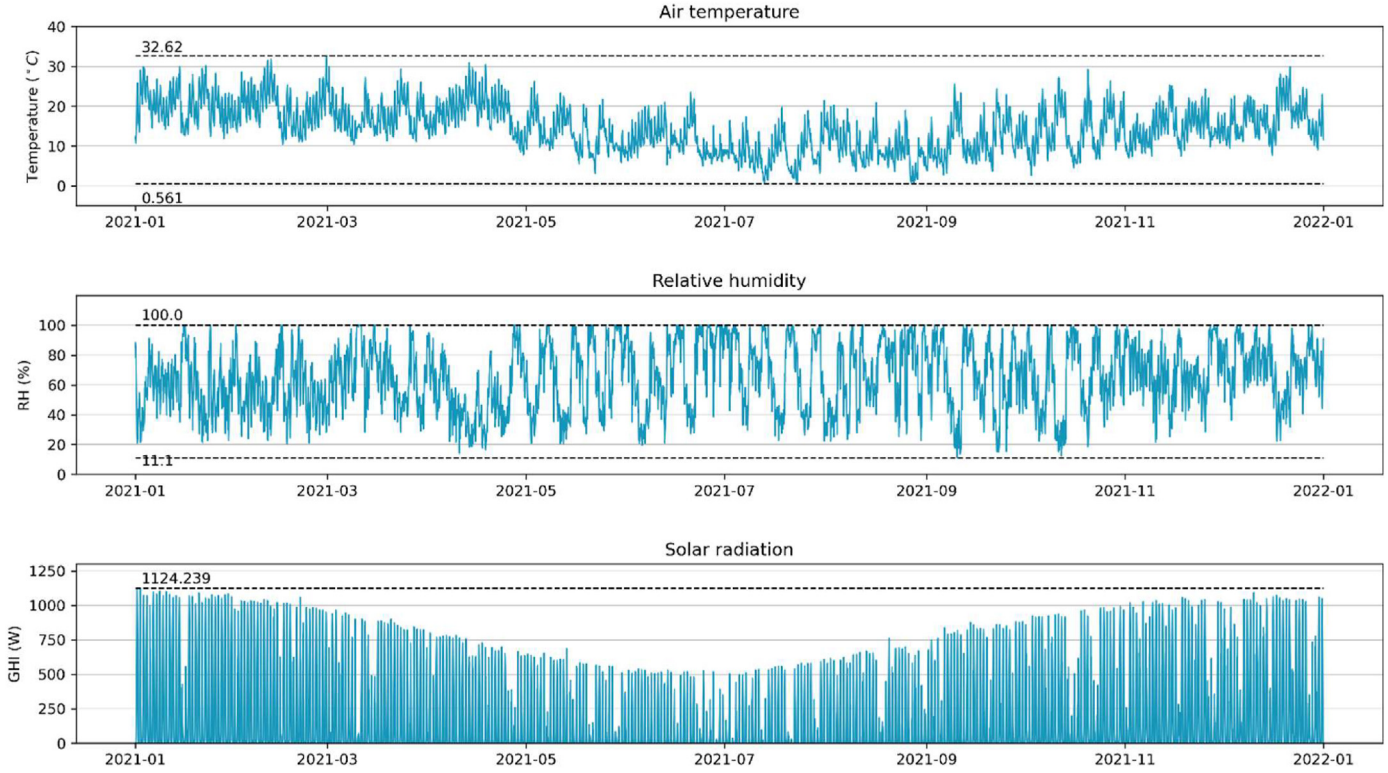

Figure 4. Air temperature, relative humidity and solar radiation for the year 2021.

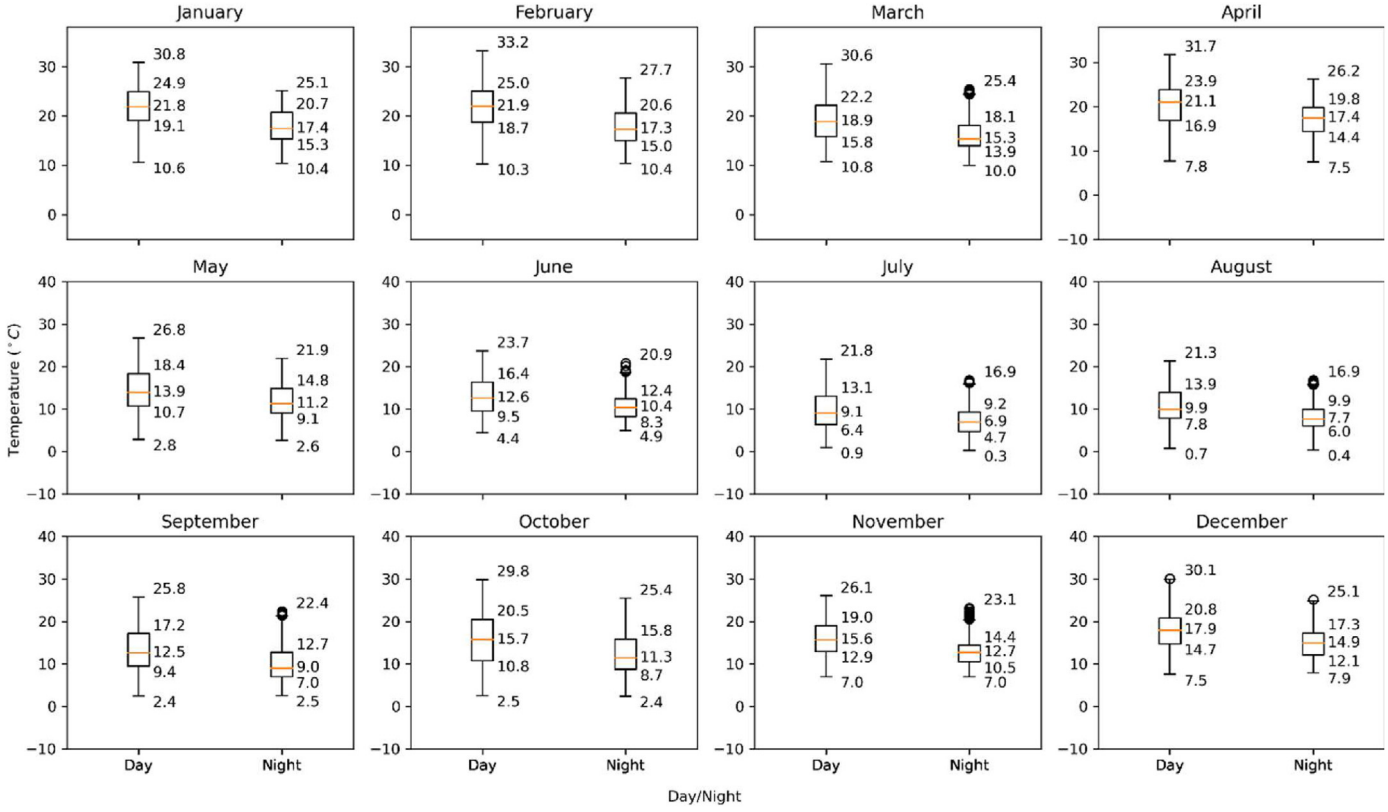

Figure 5. Monthly temperature distribution for the year 2021 at the test site.

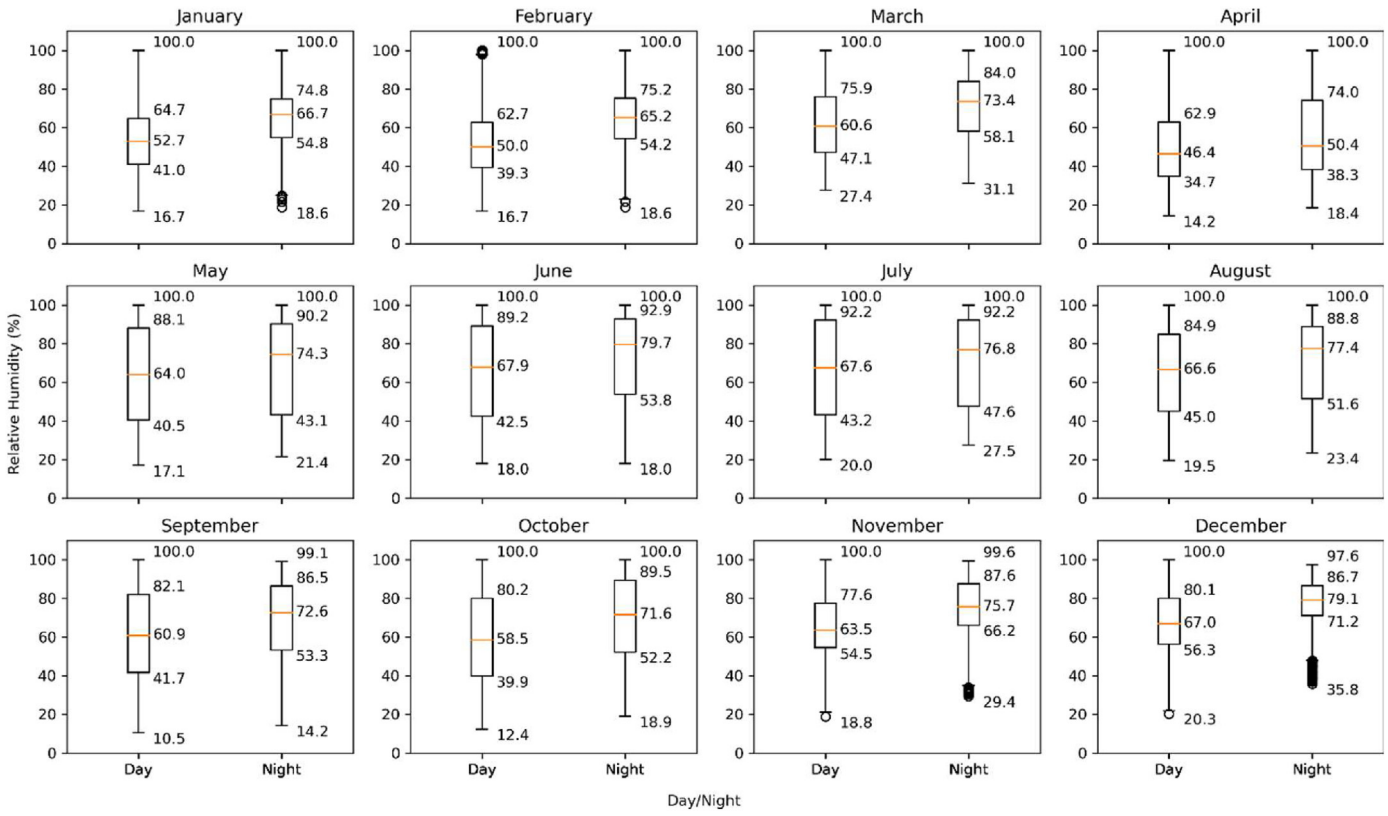

Figure 6. Monthly relative humidity distribution for the year 2021.

fourth day of the rally, clouds appear – see Figure 11. The appearance of clouds drives down the air temperature.

The top right of Figure 10 shows another absolute humidity rally, which has different characteristics than the one on the left of Figure 10. In contrast to the first humidity rally, the second is smoother, shorter, occurs at lower air temperatures and lower solar radiation. The absolute humidity increases from a value of 5 g/m^3 on 9 March to a value of 12.5 g/m^3 on 10 march. The relative humidity increases to 100 % at the end of the first day of the rally, leading to light precipitation. During this period the temperature remains fairly constant at 15 °C. Clouds are present from day one of the rally – see Figure 12. Global horizontal irradiance does not increase above 100 W/m^2 on the second day.

The humidity rallies shown in Figure 10 illustrate the interplay between absolute humidity, relative humidity, temperature and solar radiation.

Interesting to note in the solar radiation profiles on the left of Figure 10 is a 'knee' that occurs in the afternoons, on the otherwise symmetrical radiation profile. This could be explained by the fact that the weather station is located close to the mountain on the west side of the valley, thereby experiencing early shading in the afternoon.

3.2.2. Average day

Figure 13 shows the average temperature per hour, over the period of 24 h, calculated from data for January, February and March. This figure illustrates the average shape of the temperature profile during these summer months. Figure 14 shows the average relative humidity profile, while Figure 16 shows the average absolute humidity profile for January, February and March.

The temperature profile illustrated in Figure 13 indicates the temperature at four different heights above the ground: 10 cm, 45 cm, 80 cm, and 115 cm. During the night, the lowest temperature occurs, on average, closest to the ground with the highest temperature measured furthest away from the ground. During the day the lowest temperature occurs, on average, the furthest away from the ground, while the highest temperature is measured closest to the ground.

The temperature lines only cross at two distinct points: about two hours after sunrise, and about an hour before sunset. These points are both inversion points for the temperature, as well as inflection points in the shape of the temperature profile: the profile changes from convex to concave in the morning and concave to convex in the afternoon. The temperature profile during the early parts of the night (sunset to 00:00) also seems to have a higher curvature than the temperature profile during the early morning (00:00 to sunrise).

The temperature remains, on average, stratified during the night and during the day. The temperature lines invert completely when they cross: the point of lowest temperature during the night becomes the point of highest temperature during the day, the point of second lowest temperature during the night becomes the point of second highest temperature during the day, the point of second highest temperature during the night becomes the point of second lowest temperature during the day, and the point of highest temperature during the night is also the point of lowest temperature during the day.

Further considering the different stages during a 24-hour cycle (nighttime, dawn, sunrise, daytime, solar noon, dusk, and sunset) the following can be noted: temperatures gradually decrease during the night, reaching a minimum just before sunrise, with a subsequent sudden increase at sunrise. The rate of temperature increase is related to the position of the temperature measurement. Points closer to the ground experience higher rates of increase. The slope of the temperature profile suddenly increases further about an hour after sunrise. Again the rates of increase remain highest for points closer to the ground. Towards solar noon, the temperature curves start to decrease in slope. Temperatures peak at 15:00, about three hours after solar noon. The subsequent decrease in temperatures proceeds at a higher rate for points closer to the ground than for

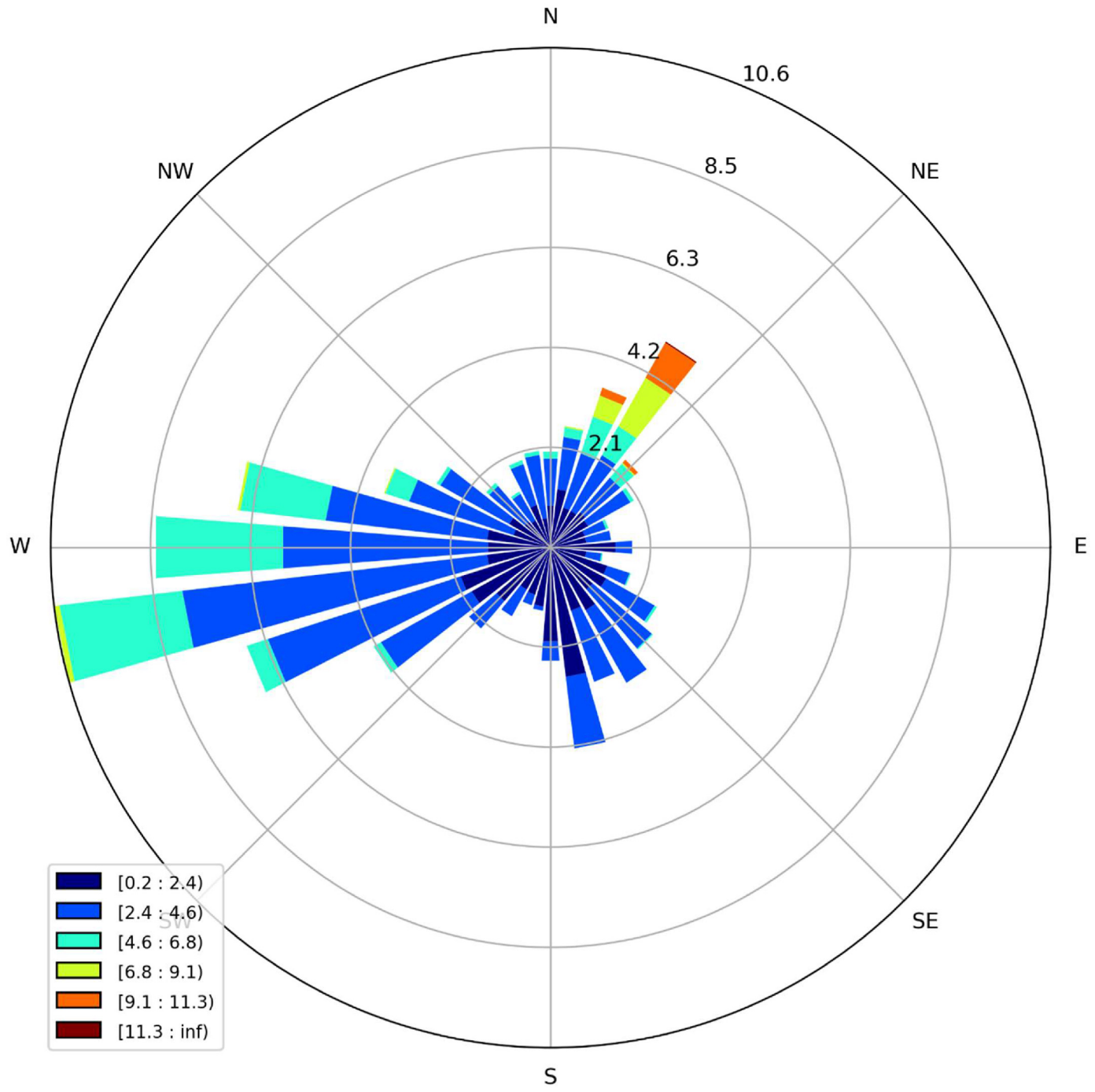

Figure 7. Subset of wind data for high absolute humidity (above the third quartile). Windspeed is in m/s.

points further away, leading to the inversion point about an hour before sunset. It is clear that the range of temperatures is largest closest to the ground, while it is less severe further away from the ground.

The inverse relationship between relative humidity and temperature is visible by comparing Figure 14 and Figure 13. On average, at all four the sampled heights above ground, the relative humidity follows the inverse pattern of the temperature: the relative humidity increases during the night, with a maximum value at sunrise, and a sudden onset of decreasing behaviour after sunrise. The relative humidity is highest close to the ground during the night, and lowest close to the ground during the day. The slope rate of change in relative humidity is also highest closes to the ground.

The relative humidity reaches a minimum at around 16:00, about an hour after air temperature reaches a maximum. It then starts a period of steep increase, which flattens off at around 21:00. Another observation is that the period between the inversion point at 17:00 and 00:00 is characterised be a hyperbolic relative humidity profile, while the period between 00:00 and sunrise is more linear (this was also observed with the temperature profile). As with the temperature profile, the relative humidity profile switches concavity when the lines invert at 07:00 and 17:00.

Figure 15 shows the average relative humidity for January, February and March, at the different sampling heights, during the day and during the night.

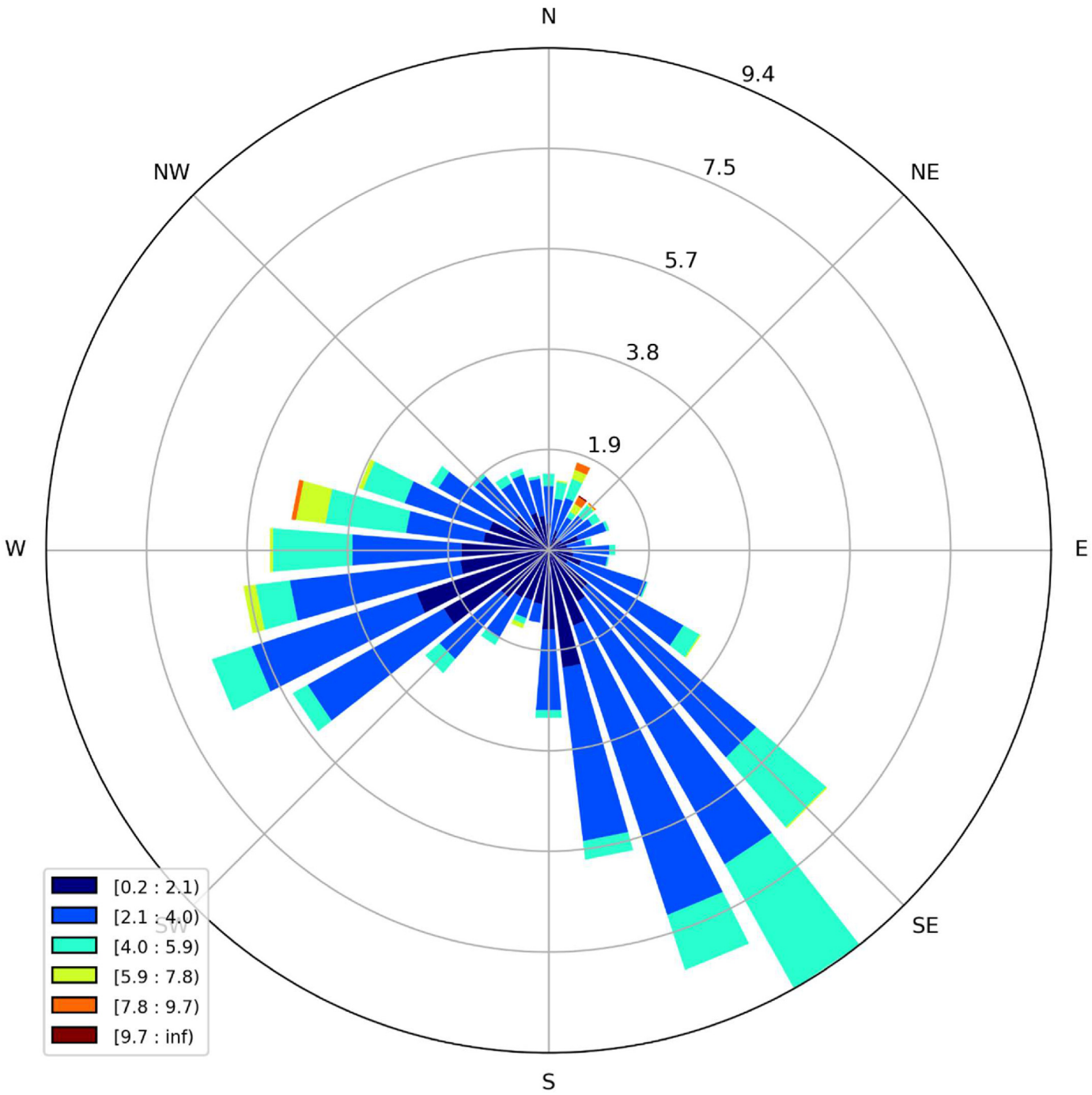

Figure 8. Subset of wind data for low absolute humidity (below the first quartile). Windspeed is in m/s.

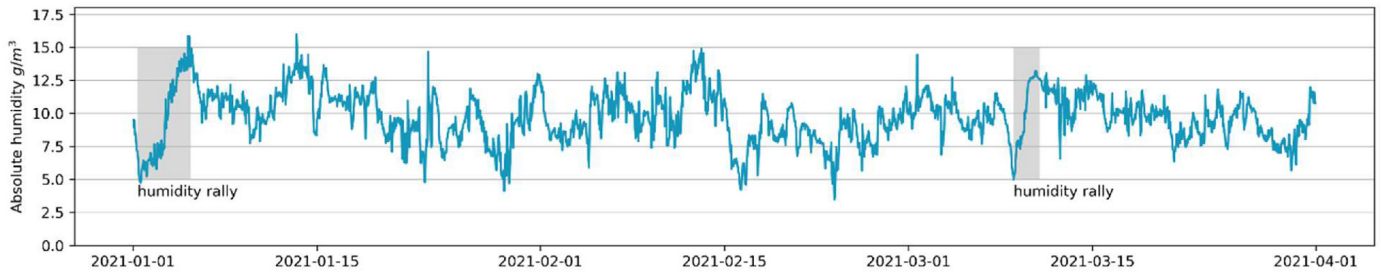

Figure 9. Absolute humidity for the period 1 January to 31 March 2021. Two humidity rallies are indicated in grey.

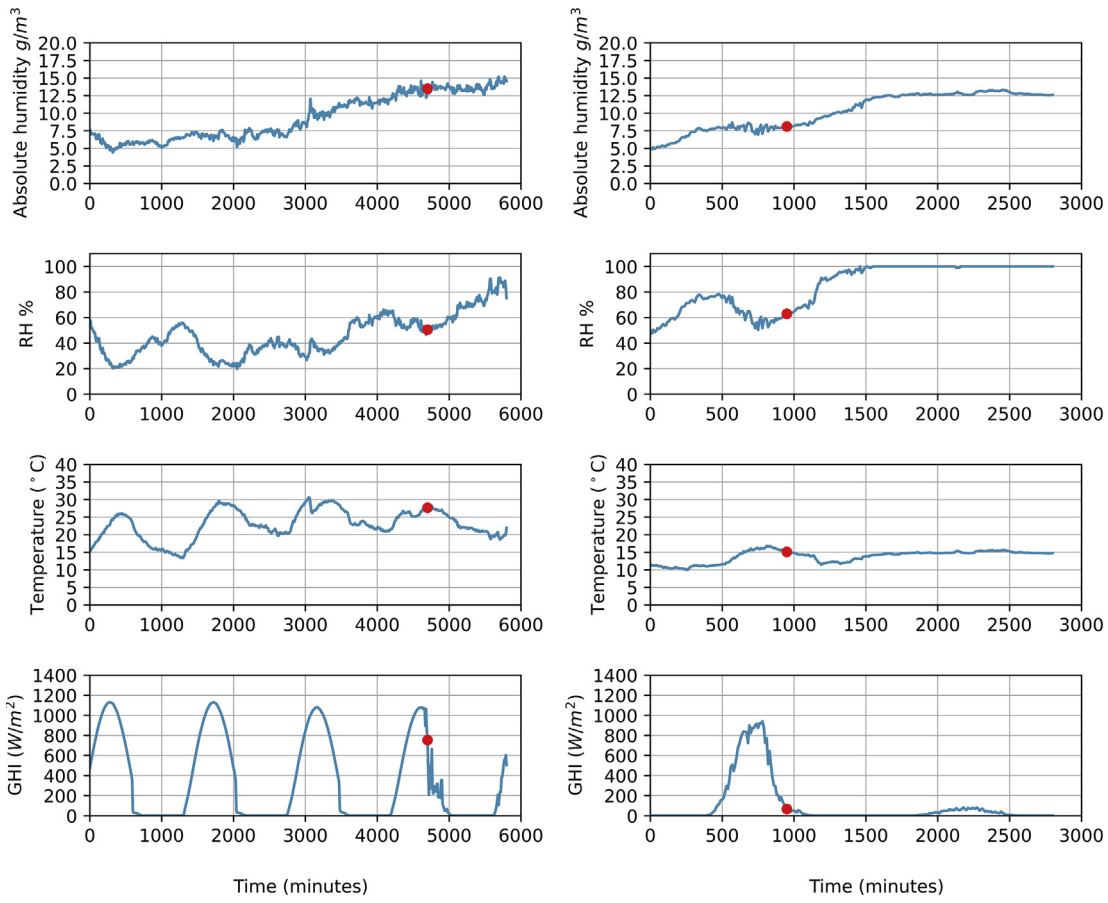

Figure 10. Absolute humidity rallies plotted with corresponding relative humidity, temperature and solar radiation. These rallies are indicated in grey in Figure 9. The red dots indicate the points at which the pictures in Figure 11 and Figure 12 were taken.

Figure 11. Picture taken by the humidity stack camera towards the end of the humidity rally, indicated with the red dot on the left of Figure 10. Clouds are starting to form. Temperature: 27.67 °C; relative humidity: 50.5%; wind: 3.26 m/s N; GHI: 753.83 W/m^2.

Figure 12. Picture taken by the humidity stack at the point indicated by the red dot on the right of Figure 10. Cloud cover is starting to form. Temperature: 15.1 °C; relative humidity: 62.9%; wind: 8.58 m/s N-E; GHI: 65.87 W/m^2 .

In order to observe the absolute change in humidity, the absolute humidity was calculated for the average day in January, February and March. This is plotted in Figure 16. The stratification of absolute humidity is not as pronounced at it is with temperature and relative humidity. Especially during the night, the absolute humidity is similar at the four sampling heights. It is the case, however, that the humidity is largest furthest from the ground during the night and largest closest to the ground during the day. The difference in humidity at different heights is more pronounced during the day than during the night. As with average temperature and relative humidity, inversion points do exist, but are less pronounced, especially in the afternoon.

A sharp decrease in absolute humidity is observed at sunrise, with a minimum about an hour after sunrise, at 06:00. The absolute humidity then increases, reaches a local maximum just before solar noon, decreases until 15:00 (which co-insides with the maximum temperature), after which it increases again to reach a global maximum at around 18:00. The absolute humidity then decreases sharply, reaching a sudden plateau at sunset. Absolute humidity is higher, on average, during the day than during the night.

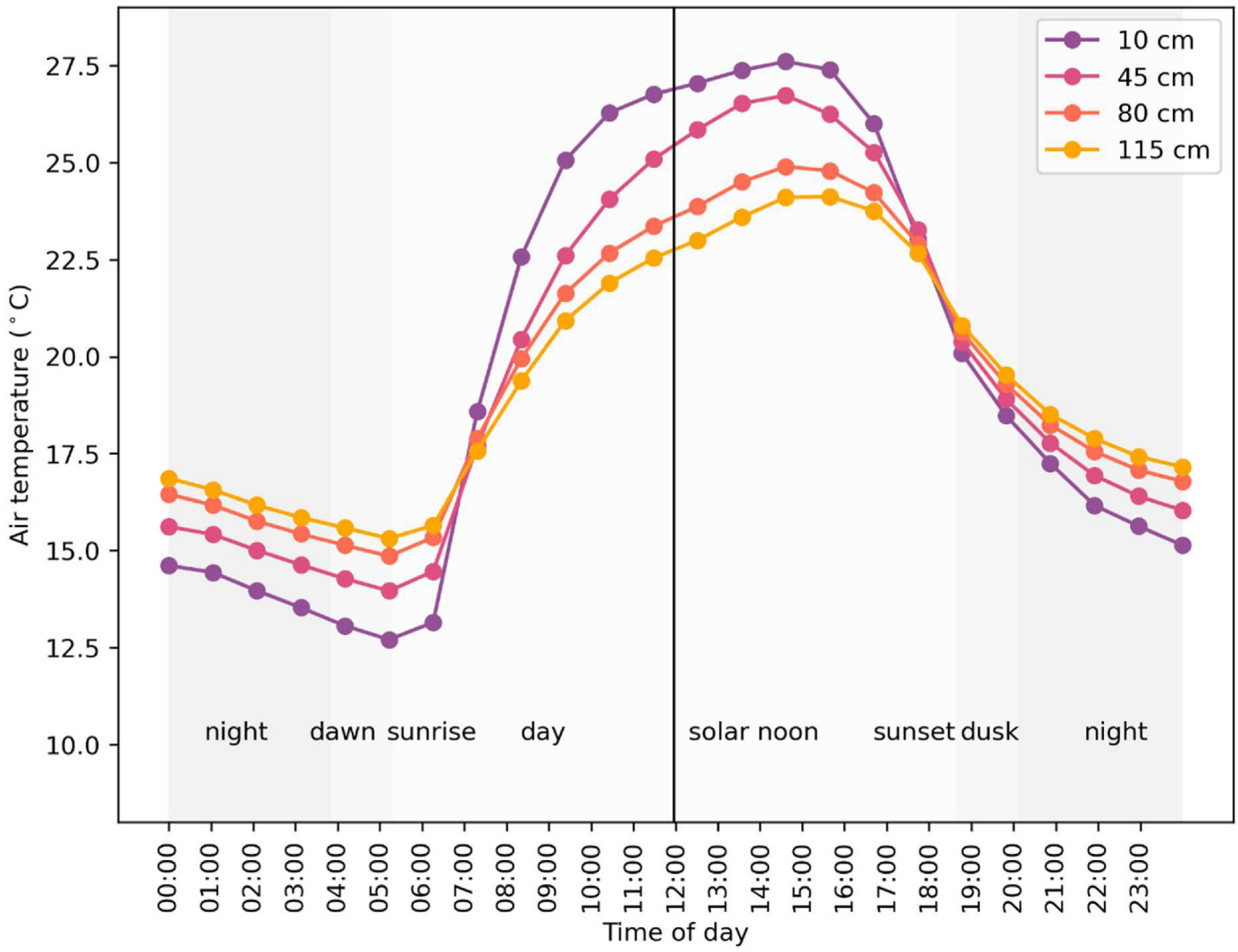

Figure 13. Average temperature profile for January, February and March 2021.

Important to note in the absolute humidity profile is the regular occurrence, in the afternoon, of local maxima and minima. This is in contrast to the more smooth profile during the first part of the day (06:00 to solar noon). This phenomena might be related to the scattering of wind speed and direction, which is also observed for the same time period (see Figure 17).

Figure 17 shows the wind roses for the average conditions every hour from 12:00 till 24:00 during January, February and March 2021. The length of each spike of the wind rose represents the frequency of the wind speed from a specific direction, the direction of the spike represents the wind direction, and the colour represents the wind speed.

Between 00:00 and 01:00 the wind blows predominantly from the west and the south (top left of Figure 17). The westerly wind becomes less dominant in the early morning as the southern component increases in dominance until 07:00. The wind direction then shifts slightly east and remains that way until 10:00. At 11:00, the westerly direction suddenly becomes prominent again. The south-easterly wind diminishes, leaving the westerly direction to dominate until 14:00. The period between 14:00 and 18:00 sees a scattered wind pattern. The onset of the scattering of the wind direction coincides with the maximum air temperature and subsides at sunset, between 18:00 and 19:00. The period between 19:00 and 23:00 sees a dominant westerly flow of wind. Between 23:00 and 00:00 a north-easterly wind develops, which diminishes again between 00:00 and 01:00.

The scattered wind direction observed in the afternoon might be explained by the fact that different geographical objects, such as dams, rocks, mountainside, and apple orchards, in the vicinity of the weather station, have varying heat capacities. This might cause an uneven distribution in air temperature across the microclimate, leading to scattered wind directions. As the heat transfer proceeds across the microclimate via convection, the distribution of air temperature becomes more even in the late-afternoon, leading to a decrease in wind scattering.

3.2.3. *Wavelet transform coherence analysis*

The microclimate dynamics introduced in Section 3.2.1 and Section 3.2.2 can be better understood by making use of wavelet transform coherence analysis. The wavelet transform coherence analysis provides further insight on which an optimized control strategy for air-based solar hydrogen production can be developed.

In order to expand on the foundation for the development of a control strategy for air-based solar hydrogen production, this section concludes with a WTC analysis based on comparing relative humidity for different heights above the ground as well as relative humidity against temperature for different heights (Gouhier et al., 2018). The dataset used for this

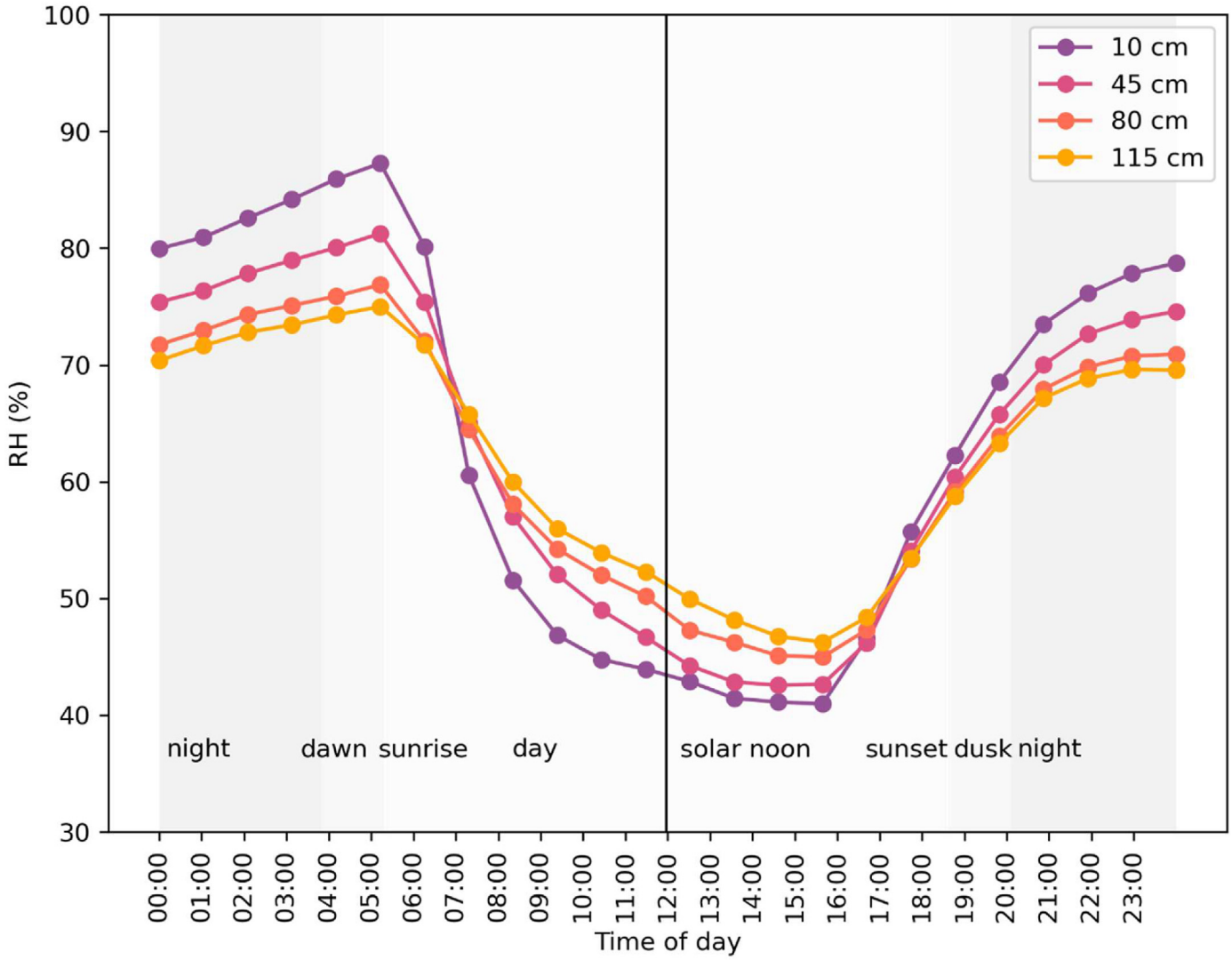

Figure 14. Average relative humidity profile for January, February and March.

analysis spans all of the seasons encountered during the year 2021 for the test site described previously in the paper, specifically starting on 00:00:00 on 2021-01-01 and concluding on 09:00:00 on 2021-11-29.

Figure 18 is the result of a WTC analysis of relative humidity at 40 cm above the ground and relative humidity at a height of 10 cm above the ground. Figure 19 is the result of a WTC analysis of temperature and relative humidity (both at a height of 10 cm above the ground).

The most prominent observations drawn from Figure 18 and Figure 19 are the strong levels of coherence between temperature and relative humidity. Relative humidity at different heights are mostly in phase, but temperature and relatively humidity at the same height are mostly out of phase. Semi-periodic islands of strong and weak coherence are observed possibly due to short time scale dynamics influencing the levels of coherency and could be considered highly unreliable regions for the purposes of inference or forecasting. Emphasis is placed on the ability of the WTC to showcase swings (or phasor evolutions) in phasor information, that is, instances where the time delay (or phase) between metrics of the microclimate change.

The value of WTC techniques, from the perspective of relating microclimate dynamics to optimal control strategies of air based solar hydrogen production, culminates in the ability to infer strategies from

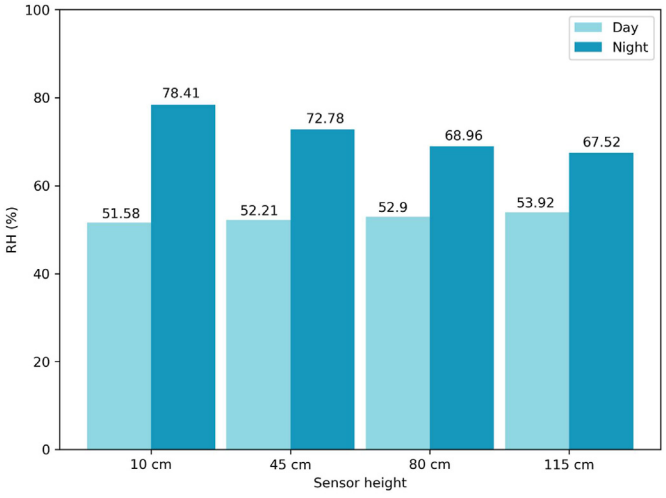

Figure 15. Average relative humidity during the day and night for January, February and March, at different sampling heights.

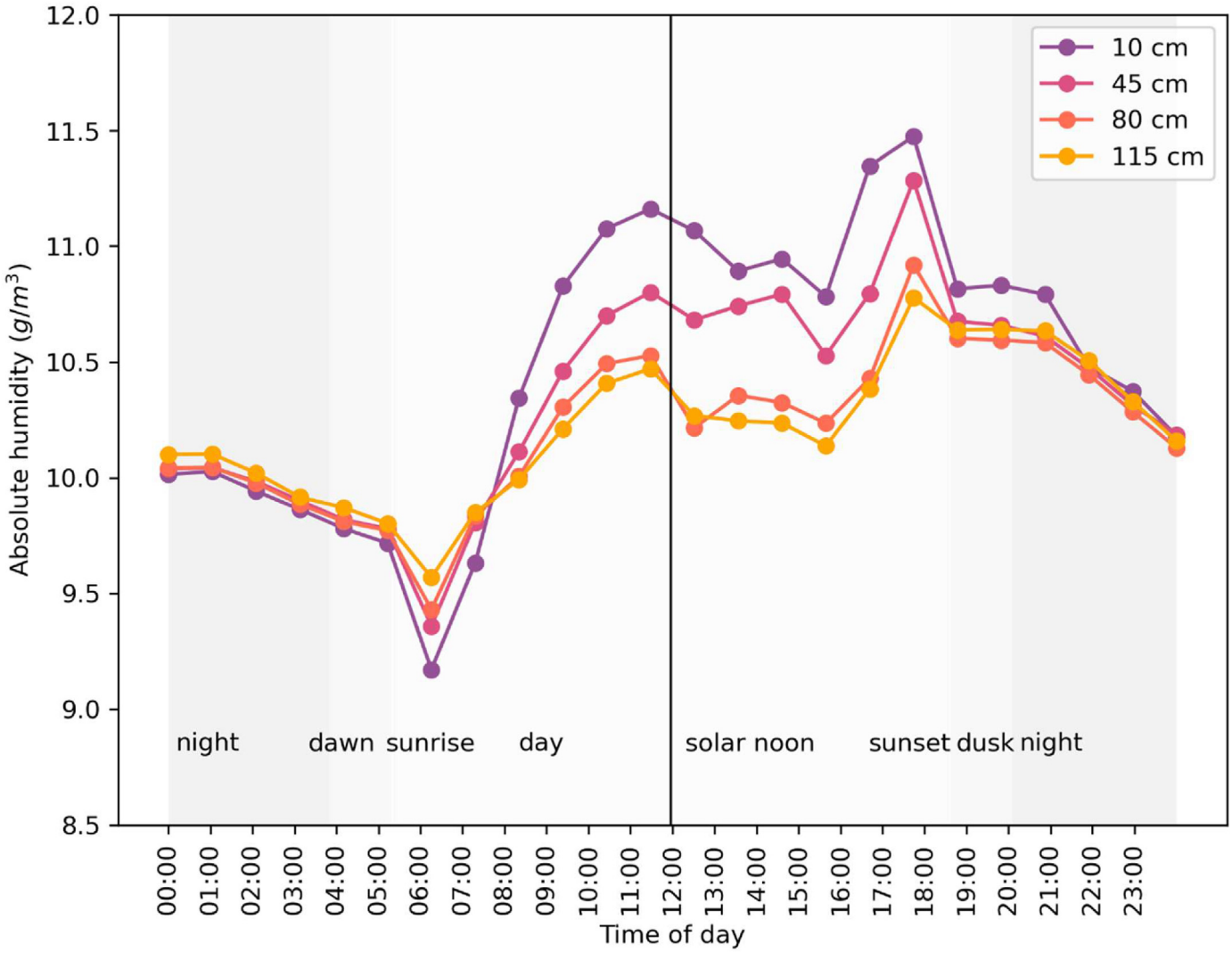

Figure 16. Absolute humidity profile for January, February and March.

the evolution of phasors associated with coherent microclimate metrics. The ability to predict the evolution of the leading/lagging attributes between microclimate metrics, could enable operators to minimize the response time to demand during certain times of the year. WTC maps could be used in conjunction with surface water and energy balances to enable further correlations.

4. Framework recommendation

A combined map of weather parameters and a WTC of relative humidity and air temperature could provide an integrated perspective of the characterization of the microclimate. Such a map enables operators to infer strategies for optimal air-based solar hydrogen production, considering the following:

4.1. Monitoring of phasor evolution

Moments of significance in phasor evolution are defined as deviations from perfect in-phase and out of phase signals, i.e. observed rotation in the phasor angle over time (as observed in Figure 18 and Figure 19). Operators can choose operating scales (from days to months, depending on generation frequency and demand) and infer the phasor status for a particular month, week or day, based on historic data, by making use of the WTC analysis. Phasors will enable the operator to determine lead or lag times between critical temperature and humidity events for a particular microclimate associated with the air-based solar hydrogen production plant.

Consider an example of the latter strategy where the operator inferred a possible phase angle of $-\pi/4$ for a particular week dominating the microclimate. With this prior knowledge (with some certainty), the operator knows that events observed in the relative humidity time series lead temperature events by some time, allowing the operator to respond changes in microclimate, in advance.

4.2. Using a combined map

Operators can correlate regions of interest, identified on the WTC map, with a water and energy balance associated with the microclimate. This will allow operators to relate primary microclimate metrics (such as temperature and relative humidity) to surface energy and water balances to enable operators to note possible ground humidity reservoirs due to surplus ground water storage associated with the air-based solar hydrogen plant. The operator will be able to compensate lead/lag times between temperature and humidity metrics by including additional dynamics due to humidity reservoirs from the ground or even nearby dams. The observed stratified nature of relative humidity and temperature (Figure 13 and Figure 14), combined with areas on the WTC map where relative humidity moves in phase at different heights above the ground,

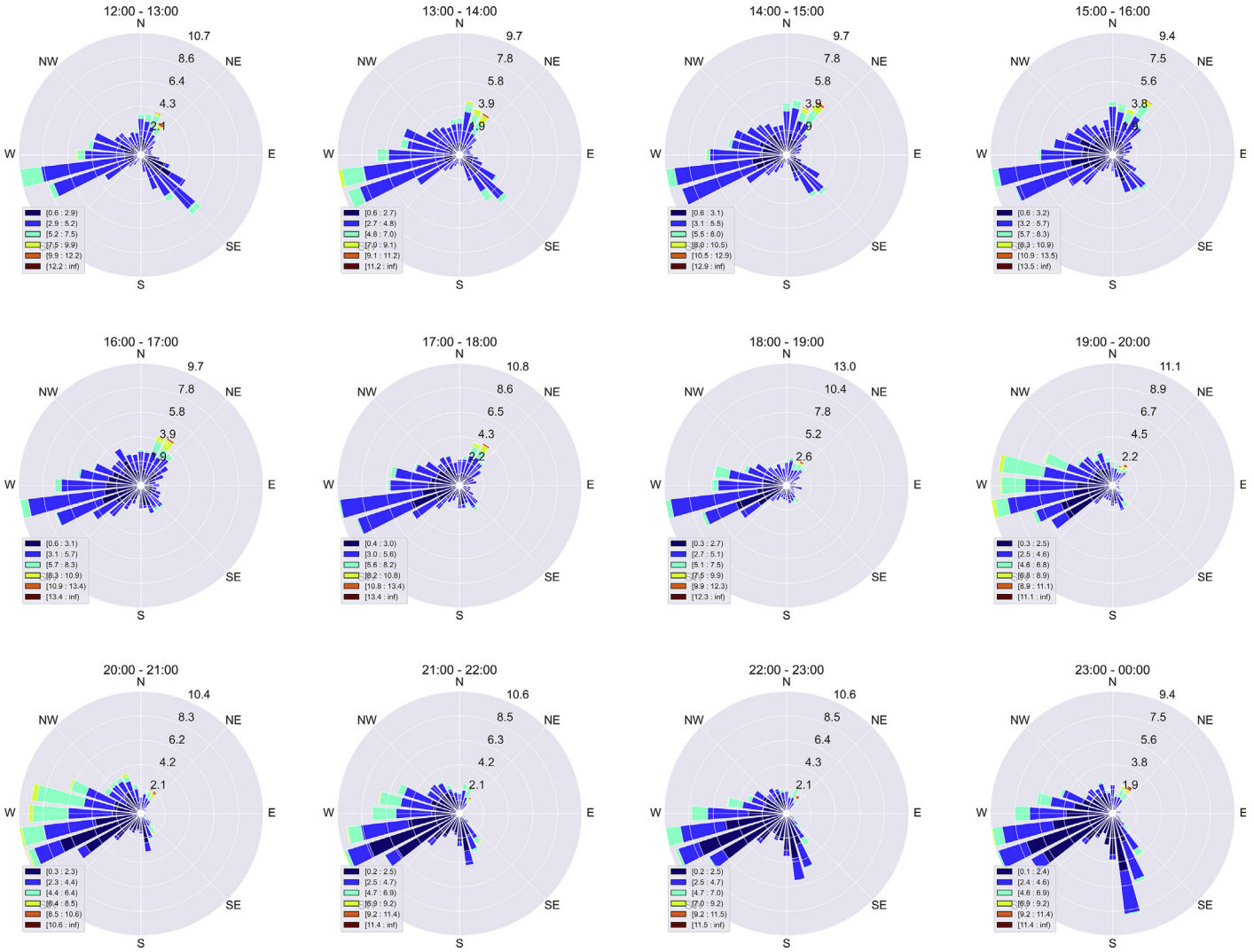

Figure 17. Wind speed, direction, and frequency on average from 12:00 till 24:00 during January, February and March 2021.

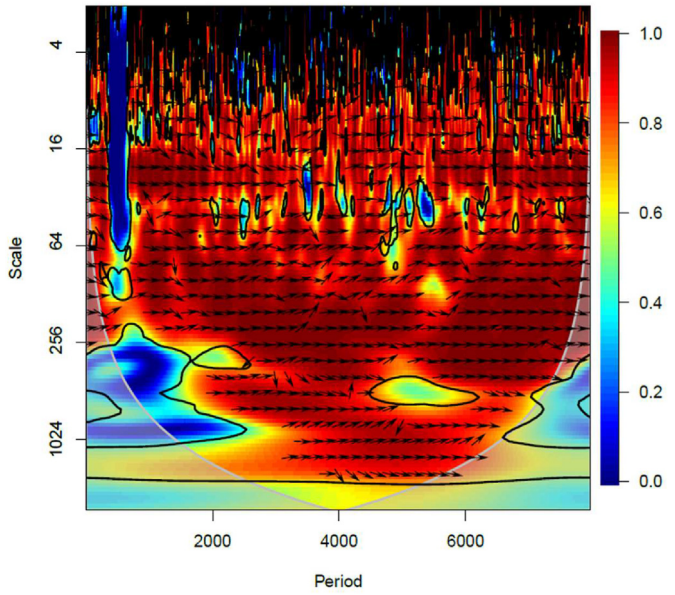

Figure 18. WTC of relative humidity (at a height of 40 cm above the ground of the testing site) and relative humidity (at a height of 10 cm above the ground of the testing site). Clear coherence and aligned phasor indications can be observed for the entire dataset. WA scales relate to the compression of the wavelet and small and large scales resemble short and long-term dynamics.

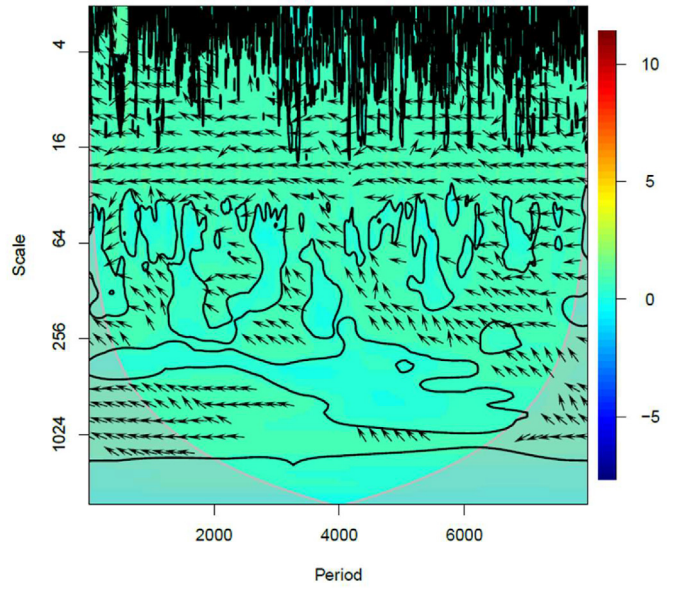

Figure 19. WTC of temperature (at a height of 10 cm above the ground of the testing site) and relative humidity (at a height of 10 cm above the ground of the testing site). Clear coherence and anti-aligned phasor indications can be observed for entire dataset. WA scales relate to the compression of the wavelet and small and large scales resemble short and long-term dynamics.

points to a humidification process that propagates horizontally, rather than vertically. Periods where the humidification process propagates primarily from the ground (for example the release of moisture from the soil) can be identified by areas were the wavelet transform coherence analysis indicates a slightly out-of-phase relation between relative humidity closer to the ground and relative humidity further away from the ground. Furthermore, the propagation direction of the humidification process can be induced from the wavelet transform coherence analysis by considering the phase angles (leading/lagging) for relative humidity at different heights above the ground.

4.3. Using islands of high/low coherence and the significance there-of

Certainty levels associated with strategies inferred from monitoring phasor evolution and using a combined map (as discussed in Section 4.1 and Section 4.2) can be enhanced by historically identifying regions where coherence is low and unstable (see for instance the horizontal strip around a scale of 64 on Figure 19). Low coherence is also observed when considering intraday variability (small WTC scales) where microclimate dynamics become unpredictable due to complex dynamics.

5. Conclusion

This paper proposes the use of a novel combination of different perspectives on location specific microclimate for the purposes of air-based solar hydrogen production management, incorporating microclimate characterization and microclimate dynamics (via the use of wavelet transform coherence techniques) to suggest a basis for an optimal control strategy for the use of the plant operator. The proposed strategy depends on historic microclimate data of which the level of certainty scales sensitively with the accuracy, depth and record interval of the historic data. Machine learning techniques can typically further automate and enhance the proposed strategy.

The data collected during 2021 was used to characterise the climatic resource by means of parameter distributions for each month, as well as time-series plots of temperature, relative humidity and solar radiation. Windroses were used to characterise the wind resource.

On the microclimate level, the relative humidity and temperature were measured at different heights above the ground, and it was found that the relative humidity is, on average, highest closest to the ground at night, and lowest closest to the ground during the day. The air temperature and relative humidity remain stratified and exhibit inversion as well as inflection points at clearly defined times of the day, which coincide with the position of the sun. The rate of change in temperature and relative humidity was found to be higher for sampling points closer to the ground. Different periods of the average day can also be defined based on the slope of the temperature profile. The shadow effect of the mountain in the afternoon is visible in the solar radiation profile, on sunny days, in the form of a knee in the otherwise symmetrical radiation profile.

The stratification of absolute humidity is not as pronounced as it is with temperature and relative humidity. Especially during the night, the absolute humidity is similar at the four sampling heights. It is the case, however, that the humidity is largest furthest from the ground during the night and largest closest to the ground during the day. The difference in humidity at different heights is more pronounced during the day than during the night. As with average temperature and relative humidity, inversion points do exist, but are less pronounced, especially in the afternoon. Absolute humidity is higher, on average, during the day than during the night.

There also seems to be a relationship between absolute humidity and wind direction, with high absolute humidity (above the third quartile) being accompanied by a westerly wind, while absolute humidity levels below the first quartile was accompanied by south-easterly winds. A correlation between air temperature and wind scattering was also noticed, with scattering occurring, on average, after the average maximum air temperature has been reached (at around 15:00). This might be explained by the difference in heat capacity of different geographical features in the vicinity of the weather station. The scattering of wind speed and direction in the afternoon seems to influence the

absolute humidity, the latter showing increased volatility in the afternoon.

It was further found that wavelet transform coherence techniques (WTC) can be successfully employed to infer areas of predictability and unpredictability within the relation between relative humidity and air temperature. Long-term and short-term trends have also been exposed within the relation between relative humidity and temperature within the microclimate. The combination of microclimate weather data and WTC analysis has been suggested as a foundation upon which optimized control strategies can be developed for air-based solar hydrogen production.

Further research is required to design algorithms which implement the proposed control strategy based on real-time microclimate data. Potential cost savings and environmental impact reduction due to the application of an optimized control strategy could also be topics for future studies.

To summarize, the authors provided a comprehensive microclimate characterization using high-quality sensing equipment at relevant proximity to the ground (below 2 m) and at different heights. This characterization was followed by an analysis of microclimate dynamics and led to the demonstration of a new framework for water-from-air management. The authors also allude the possibility of using the proposed strategy for the prediction of microclimate behaviour, by making use of regions of higher-coherence on the wavelet transform coherence map.

Declarations

Author contribution statement

Foster Lubbe: Conceived and designed experiments; Performed the experiments; Analyzed and interpreted the data; Contributed reagents, materials, analysis tools or data; Wrote the paper.

Jacques Maritz: Analyzed and interpreted the data; Contributed reagents, materials, analysis tools or data.

Tom Bosserez, Jan Rongé, Johan Martens: Contributed reagents, materials, analysis tools or data.

Funding statement

This work was supported by the Industrieel Onderzoeksfonds (IOF) with a postdoctoral research grant to Tom Bosserez and the Moonshot HyPPr project of the Vlaams Agentschap Innoveren en Ondernemen (Vlaio) (Grant number: HBC.2019.0141). Johan Martens acknowledges the Flemish government for long-term structural funding (Methusalem) (Grant number: 3E150390).

Data availability statement

Data will be made available on request.

Declaration of interests statement

The authors declare no conflict of interest.

Additional information

No additional information is available for this paper.

Acknowledgements

The authors wish to thank Mr Calla du Toit and Mr Pierre van den Heever (Sun Sweet Fruit CC) for their cooperation and for hosting the experimental setup.

References

Bhandari, R., Shah, R.R., 2021. Hydrogen as energy carrier: techno-economic assessment of decentralized hydrogen production in Germany. Renew. Energy 177, 915–931. Elsevier Ltd.

Bonkaney, A.L., Seidou Sanda, I., Balogun, A.A., 2019. Wavelet analysis of daily energy demand and weather variables. J. Energy 1–7.

Bramer, I., et al., 2018. Advances in monitoring and modelling climate at ecologically relevant scales. Adv. Ecol. Res. 58, 101–161.

Daubechies, I., Grossmann, A., Meyer, Y., 1986. Painless nonorthogonal expansions. J. Math. Phys. 27 (5), 1271–1283.

Gouhier, T.C., Grinsted, A., Simko, V., 2018. R package biwavelet: conduct univariate and bivariate wavelet analyses. Available at: https://github.com/tgouhier/biwavelet.

Grinsted, A., Moore, J., Jevrejeva, S., 2004. Application of the cross wavelet transform and wavelet coherence to geophysical time series. Nonlinear Process Geophys. 11, 561–566.

Haar, A., 1910. Zur Theorie der orthogonalen Funktionensysteme. Math. Ann. 69, 331–371.

Hamiche, A.M., Stambouli, A.B., Flazi, S., 2016. A review of the water-energy nexus. Renew. Sustain. Energy Rev. 65, 319–331. Elsevier.

Heremans, G., et al., 2017. Vapor-fed solar hydrogen production exceeding 15% efficiency using earth abundant catalysts and anion exchange membrane. Sustain. Energy Fuels 1 (10), 2061–2065.

Hydrogen Europe, 2019. Annual Report 2019.

International Energy Agency, 2021. World Energy Outlook 2021. Available at: www.iea.org/weo.

Labat, D., 2010. Cross wavelet analyses of annual continental freshwater discharge and selected climate indices. J. Hydrol. 385, 269–278. Elsevier B.V.

Lord, J., et al., 2021. Global potential for harvesting drinking water from air using solar energy'. Nature 598 (7882), 611–617. Springer US.

Miletto, M., 2015. Water and energy nexus: findings of the world water development report 2014. In: Hydrological Sciences and Water Security: Past, Present and Future, pp. 93–99.

Morecroft, M.D., Taylor, M.E., Oliver, H.R., 1998. Air and soil microclimates of deciduous woodland compared to an open site. Agric. For. Meteorol. 90 (1–2), 141–156.

Peeters, R., et al., 2021. Fresh water production from atmospheric air: technology and innovation outlook. iScience 24 (11), 103266.

Penedo, S.R.M., Netto, M.L., Justo, J.F., 2019. Designing digital filter banks using wavelets', *Eurasip Journal on Advances in Signal Processing*. EURASIP J. Appl. Signal Process. 33.

Pinaud, B.A., et al., 2013. Technical and economic feasibility of centralized facilities for solar hydrogen production via photocatalysis and photoelectrochemistry. Energy Environ. Sci. 6 (7), 1983–2002.

Rongé, J., et al., 2015. Solar hydrogen reaching maturity. Oil Gas Sci. Technol. 70 (5), 863–876.

Van De Krol, R., Liang, Y., Schoonman, J., 2008. Solar hydrogen production with nanostructured metal oxides. J. Mater. Chem. 18 (20), 2311–2320.

Yang, X., et al., 2013. Evaluation of a microclimate model for predicting the thermal behavior of different ground surfaces. Build. Environ. 60, 93–104. Elsevier Ltd.

Zhang, Q., Liu, T., 2010. Research on mid-long term load forecasting base on wavelet neural network. In: 2010 2nd International Conference on Computer Engineering and Applications, ICCEA 2010. IEEE, 2, pp. 217–220.